Available online at www.sciencedirect.com
SCIENCE DIRECT®
Journal of Sound and Vibration 290 (2006) 991–1014
JOURNAL OF SOUND AND VIBRATION
www.elsevier.com/locate/jsvi

Optimal stochastic models for spacecraft atmospheric re-entry

R.V. Field Jr.[a,*], M. Grigoriu[b]

[a]*Structural Dynamics Research Department, Sandia National Laboratories, Albuquerque, NM, USA*
[b]*School of Civil & Environmental Engineering, Cornell University, Ithaca, NY 14853, USA*

Received 24 November 2004; received in revised form 26 April 2005; accepted 3 May 2005
Available online 25 July 2005

Abstract

A method is developed and applied to select optimal models for loads encountered during the atmospheric re-entry of a spacecraft. In general, information on the re-entry environment is limited, meaning that two or more models for this environment may be consistent with the available information. This defines a collection of candidate models; each model in the collection is consistent with the available information. Methods from decision theory are applied to select the optimal member from the collection. A performance criterion, based on postulated utility functions, is used in the selection process. Herein, we model the re-entry environment as a stochastic process in both space and time. Information on the probability law of the process is limited. The candidate models form a class of non-Gaussian, stationary, stochastic processes. It is shown that the response of a critical internal component is sensitive to assumptions on the unknown properties of the input; the response of the component is therefore used as the performance criterion to select an optimal model for the re-entry environment.

1. Introduction

Atmospheric re-entry is concerned primarily with the passage of ballistic objects through the Earth's atmosphere [1]. All space vehicles that are required to return to Earth must endure the extreme environment associated with atmospheric re-entry. This environment includes the effects of aerodynamic heating, large rates of deceleration, radiation effects, and loads due to shock and

*Corresponding author. Tel.: +1 505 284 4060; fax: +1 505 844 9297.
E-mail addresses: rvfield@sandia.gov (R.V. Field Jr.), mdg12@cornell.edu (M. Grigoriu).

0022-460X/$ - see front matter © 2005 Elsevier Ltd. All rights reserved.
doi:10.1016/j.jsv.2005.05.007

vibration [2]. While all of these effects must be considered in typical spacecraft design, the work presented here is concerned only with the vibrational effects of the re-entry environment. The remaining effects can be incorporated into the proposed framework for model selection.

At high speeds encountered during atmospheric re-entry, the in-flight vibration response of a spacecraft is primarily due to external fluctuating pressure loads, which result from unsteady aerodynamic flows over the vehicle [3]. The role of the structural/mechanical engineer is to ensure that all internal components of the spacecraft, e.g., electronics, astronauts, etc., survive atmospheric re-entry. Typically, this means that the internal components must continue to operate normally with a prescribed level of reliability. To do this requires models of the spacecraft and the re-entry environment, where the latter is a characterization of the applied pressure loads in space and time. Due to the severity of this environment, it is nearly impossible to attain experimental data, and the characteristics of the excitation remain largely undefined. Usually, assumptions are made about the missing information so an analysis can be completed; the consequences of these assumptions are, in general, difficult to quantify.

We model the pressure field as a stochastic process in space and time, and examine the effects of two missing pieces of information: (1) the spatial correlation of the process, and (2) the marginal distribution function of the process. A decision-theoretic method for model selection, developed in Refs. [4,5], is used to select the optimal model from a class of candidate models for the spatial correlation and marginal distribution of the applied pressure field.

Typically, the assessment of the structural response of a spacecraft during atmospheric re-entry is limited to second-moment analysis [3,6,7] and [8, Chapter 10]. For structural reliability calculations, this requires one to assume the marginal distribution function of the applied pressure field to be Gaussian. Consider Fig. 1, which shows actual accelerometer data recorded during the initial portions of the re-entry phase of mission STS-62 of the NASA Space Shuttle Orbiter [9]. Shown are the accelerations of the center of mass of the Orbiter in three directions as a function of time. The sample functions shown in Fig. 1 clearly do not come from a Gaussian process. In addition, wind tunnel pressure measurements on an aircraft fuselage are shown in Fig. 2; similar non-Gaussian behavior is noted. Non-Gaussian response (Fig. 1) and non-Gaussian applied pressures (Fig. 2) together suggest that the applied load during atmospheric re-entry may be non-Gaussian as well.

Consider the spacecraft depicted schematically in Fig. 3, where the random vector pressure field, $\mathbf{Z}(\mathbf{x};t)$, models the loading during atmospheric re-entry, where $\mathbf{x}$ and t denote location on the outer surface of the spacecraft and time, respectively. The spacecraft, shown here as a perfect cone, has several stiffening ribs oriented in the hoop direction; a base ring is located at the aft end of the spacecraft to provide added stiffness. An internal component, depicted by a solid circle in the figure, is connected to the skin of the spacecraft via several supports, each having structural properties, $\mathbf{k}_c$.

Two response quantities are of interest: the vector displacement response of the skin of the spacecraft, $\mathbf{D}(\mathbf{x};t)$, and the vector acceleration response of the internal component, $\ddot{\mathbf{Y}}(t)$. Models of the spacecraft and the applied pressure field can be developed based on the available information. The objective is to use these models to assess the performance of the spacecraft during atmospheric re-entry from properties of $\mathbf{D}(\mathbf{x};t)$ and $\ddot{\mathbf{Y}}(t)$.

In Section 2, we develop a 1-D model for the spacecraft; it is assumed all required information is available to construct the spacecraft model. In Section 3, the model for the applied pressure

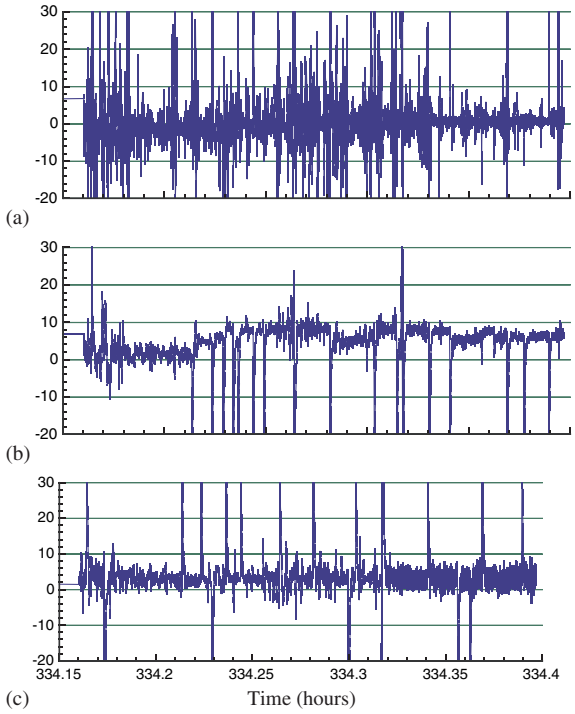

Fig. 1. Axial (a), vertical (b), and lateral (c) acceleration data from Space Shuttle mission STS-62 [9].

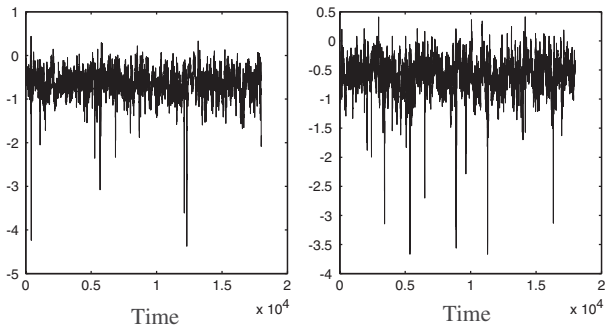

Fig. 2. Wind tunnel pressure measurements.

field, $\mathbf{Z}$, is developed. The available information on $\mathbf{Z}(\mathbf{x};t)$ is incomplete and we apply the decision-theoretic method for model selection to choose optimal models for the input in Sections 4 and 5. Because the applied pressure field is a stochastic process in both space and time, the spatial and temporal correlation functions, as well as the marginal distribution function, are necessary to define $\mathbf{Z}(\mathbf{x};t)$. Two cases are considered for illustration: (1) $\mathbf{Z}(\mathbf{x};t)$ is assumed to be a Gaussian process with partially defined spatial correlation function, and (2) $\mathbf{Z}(\mathbf{x};t)$ is assumed to be completely defined in the second-moment sense, but with unknown marginal distribution

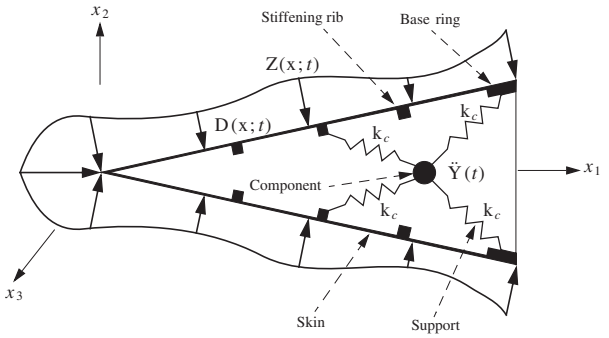

Fig. 3. Spacecraft during atmospheric re-entry.

function. The decision-theoretic method for model selection is used to select optimal models for **Z** for each case.

2. Spacecraft model

We develop the model for the spacecraft shown in Fig. 3. Two cases are considered: (i) the dynamics of the internal component and spacecraft are fully coupled, and (ii) the dynamics of the internal component depend on the spacecraft, but no feedback occurs. Methods for analysis under both cases are discussed. The available information on the spacecraft, discussed in Section 2.1, is assumed complete; Sections 2.2 and 2.3 discuss the mathematical model and methods for response analysis, respectively.

2.1. Available information

It is assumed that: (1) the spacecraft is made of a single, linear elastic material with known, deterministic modulus of elasticity, e, and mass density, μ, (2) the spacecraft geometry is a perfect cone with cone angle, α, (3) away from the stiffening ribs and base ring, the skin of the spacecraft has constant thickness, c, (4) the internal component can be modeled as a point mass with value m_c, and (5) its supports behave as simple springs with known, deterministic spring constant, $\mathbf{k}_c$.

Because of the symmetry of the spacecraft, an axial section of the cone, having width $s(x_1) = s_0 x_1$, where $s_0 > 0$ is a constant, can be formulated as a beam on elastic foundation [10]. This conical section is shown in the top of Fig. 4; shown at the bottom is α, the cone angle, and c, the skin thickness. The corresponding picture of the spacecraft is a function of a single dimension, $x_1 = x$, and is shown in Fig. 5, where $\mathbf{Z}(\mathbf{x};t) = Z(x;t)$ denotes the applied scalar pressure field, and $\mathbf{D}(\mathbf{x};t) = D(x;t)$ denotes the scalar displacement response of the beam. The quantities, Z and D are no longer in bold to denote they are now scalar quantities. The component and its support behave as a single dof oscillator located a distance b from the front of the beam, with mass, m_c, and stiffness, $\mathbf{k}_c = k_c$. The beam has total length l. The quantity $Y(t)$ represents the scalar displacement response of the component with respect to an inertial frame of reference.

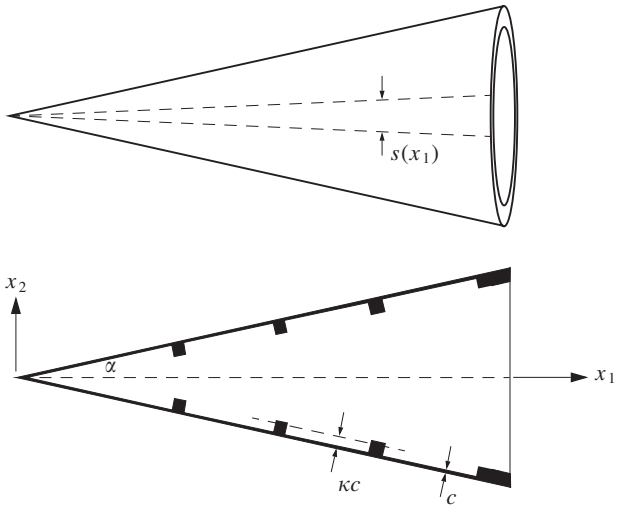

Fig. 4. Conical section of the spacecraft.

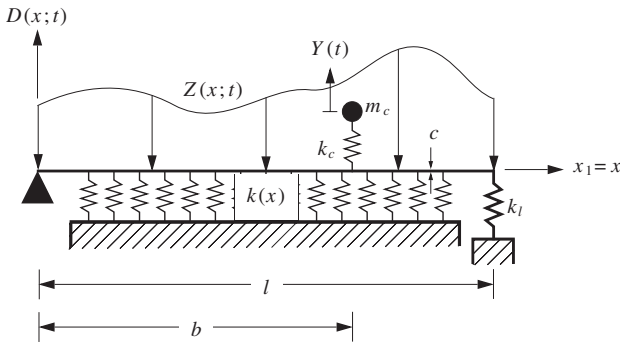

Fig. 5. One-dimensional spacecraft: beam on elastic foundation with attached oscillator.

2.2. Mathematical model

The 1-D representation of the spacecraft is a beam on elastic foundation with attached oscillator. The foundation stiffness of the beam is given by (see Ref. [10, p. 120])

$$k(x) = \frac{s_0 ec}{x \sin^2 \alpha \cos \alpha}, \quad 0 < x \leqslant l, \tag{1}$$

where the non-uniformity of $k(x)$ is due to the conical geometry of the spacecraft. At $x = 0$, corresponding to the nose of the spacecraft, the stiffness is infinite; the beam is therefore constrained in the vertical direction at $x = 0$. The beam is tapered, with cross-sectional area

$$a(x) = \frac{s_0 \kappa c}{\cos^3 \alpha} x \tag{2}$$

and bending moment of inertia

$$i(x) = \frac{s_0(\kappa c)^3}{12\cos^3\alpha}\, x, \tag{3}$$

where parameter $\kappa \geqslant 1$ is used to represent the effective thickness of the skin due to the stiffening ribs (refer to Fig. 4). The spring at the right end of the beam with stiffness $k_l > 0$ is used to represent the added stiffness of the base ring.

Let q and q_c denote viscous damping coefficients for the beam and component support, respectively. The equations of motion governing the beam deflection and position of the mass are given by [11]

$$\begin{aligned} &e[i(x)D''(x;t)]'' + \mu a(x)\ddot{D}(x;t) + q\dot{D}(x;t) + k(x)D(x;t) + k_l D(l;t)\delta(x-l) \\ &\quad = -m_c\ddot{Y}(t)\delta(x-b) - \frac{xs(x)}{2}Z(x;t), \\ &\quad m_c\ddot{Y}(t) + q_c\dot{Y}(t) + k_c Y(t) = q_c\dot{D}(b;t) + k_c D(b;t) \end{aligned} \tag{4}$$

with appropriate boundary and initial conditions. Here, $\delta(x)$ denotes the Dirac delta function, $xs(x)/2$ is the area of the top of the beam, used to convert the applied pressure, $Z(x;t)$, to a force, and $(\,)'$ and $\dot{(\,)}$ denote differentiation with respect to x and t, respectively.

Table 1 lists the values of the parameters of the spacecraft model. Parameters e and μ are consistent with the properties of aluminum. The base ring stiffness is five times the foundation stiffness at the right end of the beam, i.e., $k_l = 5k(l)$, and s_0 was selected so that $s(l) = 1$ rad. Parameters c and κ were selected to give adequate separation between the stiffness of the beam and the stiffness of the foundation.

2.3. Response analysis

Define $0 = x_1 < x_2 < \cdots < x_n = l$ to be a partition of $[0, l]$ and let

$$D_i(t) = D(x_i;t), \quad i = 1,2,\ldots,n, \quad \text{and}$$

$$\mathbf{D}(t) = (D_1(t)D_2(t)\ldots D_n(t))^{\mathrm{T}}. \tag{5}$$

Table 1
Spacecraft model parameters

Parameter	Value	Units
α	$\pi/12$	rad
κ	50	—
s_0	0.267	—
μ	2.77	g/cm^3
c	0.0635	cm
e	68950	MPa
k_l	3.5×10^5	N/cm
l	127	cm

An approximation to Eq. (4) is then given by

$$\mathbf{m}\begin{bmatrix}\ddot{\mathbf{D}}(t)\\ \ddot{Y}(t)\end{bmatrix}+\mathbf{q}\begin{bmatrix}\dot{\mathbf{D}}(t)\\ \dot{Y}(t)\end{bmatrix}+\mathbf{k}\begin{bmatrix}\mathbf{D}(t)\\ Y(t)\end{bmatrix}=\mathbf{b}\mathbf{Z}(t), \tag{6}$$

where $\mathbf{m}$, $\mathbf{q}$, and $\mathbf{k}$ are $(n+1)\times(n+1)$ matrices representing the mass, damping, and stiffness of the beam with attached oscillator, respectively, $\mathbf{b}$ is a $(n+1)\times\bar{n}$ matrix, and

$$\mathbf{Z}(t)=(Z_1(t)Z_2(t)\dots Z_{\bar{n}}(t))^{\mathrm{T}},$$

where

$$Z_i(t)=Z(x_i;t),\quad i=1,2,\dots,\bar{n} \tag{7}$$

is the input, $Z(x;t)$, discretized in the spatial dimension via partition $0=x_1<x_2<\cdots<x_{\bar{n}}=l$. The traditional finite element formulation (see, for example, Ref. [12, Chapter 16]) is used to derive $\mathbf{m}$, $\mathbf{q}$, and $\mathbf{k}$. In the analyses that follow, $n=\bar{n}=20$, parameters $b=95.25\,\mathrm{cm}$ (37.5 in), $m_c=10.9\,\mathrm{kg}$ (24 $\mathrm{lb_m}$), and $k_c=4.38\times10^5\,\mathrm{N/cm}$ ($2.5\times10^5\,\mathrm{lb/in}$) are used for calculations, and the system is assumed classically damped with 2% damping applied to each mode. Small values for n and $\bar{n}$ are used to reduce the number of calculations. We note that additional levels for model decision can be introduced by considering, for example, several dynamics models for the spacecraft, each with different values for n and/or $\bar{n}$.

If we assume negligible feedback from the mass to the beam, Eq. (6) can be simplified to

$$\tilde{\mathbf{m}}\ddot{\mathbf{D}}(t)+\tilde{\mathbf{q}}\dot{\mathbf{D}}(t)+\tilde{\mathbf{k}}\mathbf{D}(t)=\tilde{\mathbf{b}}\mathbf{Z}(t), \tag{8a}$$

$$\ddot{Y}(t)+2\zeta_c\omega_c\dot{Y}(t)+\omega_c^2Y(t)=2\zeta_c\omega_c\dot{D}_j(t)+\omega_c^2D_j(t), \tag{8b}$$

where $\tilde{\mathbf{m}}$, $\tilde{\mathbf{q}}$, and $\tilde{\mathbf{k}}$ are $\mathbf{m}$, $\mathbf{q}$, and $\mathbf{k}$, respectively, with the $(n+1)$ row and column removed, $\tilde{\mathbf{b}}$ is $\mathbf{b}$ with the $(n+1)$ row removed, and $x_j=b$. Parameters $\zeta_c=q_c/\sqrt{4k_cm_c}$ and $\omega_c=\sqrt{m_c/k_c}$ are the damping ratio and natural frequency, respectively, of the oscillator. Eqs. (6) and (8) can both be converted into a system of $2(n+1)$ linear ordinary differential equations and solved using a state–space approach; numerical solutions are provided using a fourth-order Runge–Kutta method (see Ref. [13, Section 6.3]).

3. Input model

We next develop the model of the input to the spacecraft, $Z(x;t)$. As will be shown in Section 3.1, the available information on Z is incomplete. Hence, the model for the input is not completely defined.

3.1. Available information

It is assumed that the applied pressure field can be written as

$$Z(x;t)=\sigma_Z(x)Q(x;t),\quad t\in[0,\bar{t}], \tag{9}$$

where $\sigma_Z(x)$ is a known, non-negative, deterministic function of x, $Q(x;t)$ is a weakly stationary stochastic process with partially defined second-moment properties, and $\bar{t} \geqslant 0$ denotes the duration of the re-entry event. The available information on Q, $\forall x \in [0, l]$ and $\forall t \in [0, \bar{t}]$, is given by

(1) $E[Q(x;t)] = 0$,
(2) $\mathrm{Var}[Q(x;t)] = 1$,
(3) $E[Q(x;t)Q(x+\eta;t+\tau)] = c_Q(\tau;\bar{\omega})\phi(\eta;\theta)$, where

$$c_Q(\tau;\bar{\omega}) = \frac{\sin(\bar{\omega}\tau)}{\bar{\omega}\tau}, \quad \tau \neq 0 \tag{10}$$

and

$$\phi(\eta;\theta) = \exp(-\theta|\eta|), \tag{11}$$

denote the temporal and spatial correlation functions of Q, respectively, and
(4) $\bar{\omega} > 0$ is a known, deterministic parameter.

By items (1)–(4), Q is a zero-mean, unit variance, band-limited white-noise process [14] with cut-off frequency $\bar{\omega}$. The Fourier transform of c_Q gives the power spectral density (PSD) of Q. The one-sided PSD, denoted by $g_Q(\omega)$, is shown on the left of Fig. 6 for $\bar{\omega} = 20,000$ Hz; $\sigma_Z(x)$ is shown on the right of Fig. 6. The properties for Z and Q are consistent with results from both empirical studies [15] and theoretical models [16]. The value for the spatial correlation parameter, $\theta \geqslant 0$, as well as the probability law for Z, are unknown.

3.2. Mathematical model

As illustrated in the previous section, the second-moment properties of the input, Z, are not completely defined. Information on the spatial correlation of Q and, hence, the spatial correlation of Z, is not available. In addition, nothing is known about the probability laws of Q or Z. We consider two cases for the missing information on Z, and select the optimal model for Z under each. *Case* #1: $Q = G$, where G is a Gaussian process. In this case, the only missing piece of information is the value for the spatial correlation parameter, θ; an extension to Case #1, where the functional form for ϕ, defined by Eq. (11), is unknown, is considered in Ref. [4], Section 5.7. *Case* #2: Q is a non-Gaussian process with completely defined second-moment properties. In this case, we set $\phi(\eta) = 1$, $\forall \eta \in [0, l]$, which corresponds to the limiting case of $\theta \to 0$ in Eq. (11).

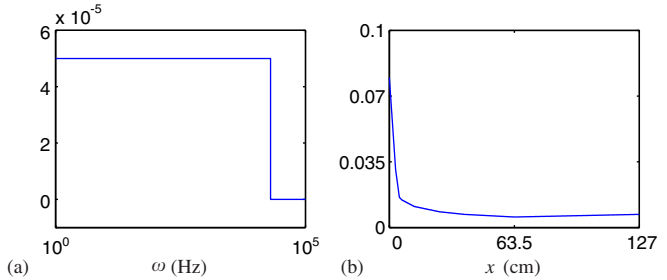

Fig. 6. Available information on Z: (a) $g_Q(\omega)$ in units of Hz^{-1}, and (b) $\sigma_Z(x)$ in units of MPa.

In Sections 4 and 5, we employ the decision-theoretic method for model selection developed in Refs. [4,5] to choose optimal models for Z for Cases #1 and #2, respectively. In each section, we first define a class of candidate models, where each member of the class is consistent with all available information on Z. Second, we illustrate that different models from the class of candidate models may have a significant impact on the properties of the response of interest. Third, we develop an appropriate utility function and use it to select the optimal model from the class of candidate models. Fourth, we study the sensitivity of the optimal model to changes in the utility function; it is assumed that the consequences of system failure are well-understood, so that any uncertainty in the definition of the utility function is limited.

The objective is to use the mathematical models for the spacecraft and the applied pressure field to assess system performance. In particular, suppose

$$g(\ddot{Y}) = \max_{t\in[0,\xi]} |\ddot{Y}(t)| \tag{12}$$

is a property of interest, where $\ddot{Y}(t) = \mathrm{d}^2 Y(t)/\mathrm{d}t^2$ and $\xi \geqslant \bar{t}$ denotes a relevant time for assessing system performance. The performance of the system is then assessed via predictions of

$$P(g(\ddot{Y}) \leqslant d), \tag{13}$$

where $d \geqslant 0$ denotes a critical value of $\ddot{Y}$.

4. Model selection for spatial correlation parameter

We employ the decision-theoretic method for model selection to choose the optimal value for parameter θ of the spatial correlation function of the applied pressure field, Z, defined by Eq. (11), i.e., Case #1.

4.1. Candidate models

Let

$$\mathscr{M}_1 = \{\theta \geqslant 0\colon \phi(\eta;\theta) = \exp(-\theta|\eta|)\} \tag{14}$$

be the collection of candidate models. This collection is uncountably infinite; we instead consider a finite sub-collection $\bar{\mathscr{M}}_1 \subset \mathscr{M}_1$, where

$$\begin{aligned}\bar{\mathscr{M}}_1 &= \{\theta_i \geqslant 0\colon \phi(\eta;\theta_i) = \exp(-\theta_i|\eta|),\ i = 1,\ldots,4\}\\ &= \{m_1(\theta_1), m_2(\theta_2), m_3(\theta_3), m_4(\theta_4)\}.\end{aligned} \tag{15}$$

The four candidate models are shown in Fig. 7. By Eq. (11), for large θ, $G(x;t)$ is nearly uncorrelated in the spatial dimension; as θ approaches zero, the process becomes perfectly correlated in space. Note that the correlation structure in time for each member of $\bar{\mathscr{M}}_1$, i.e., $E[G(x_0;t)G(x_0;t+\tau)]$ for fixed $x_0 \in [0,l]$, is given by Eq. (10).

Samples of $G(x;t)$ are shown in Fig. 8 for each of the four values for θ considered; methods from Ref. [17, Section 4.3.2], were used to generate the samples. Each plot shows $G(x;t)$ at $x = 25.4\,\mathrm{cm}$ (10 in), denoted by a solid line, and $x = 95.25\,\mathrm{cm}$ (37.5 in), denoted by a dashed line,

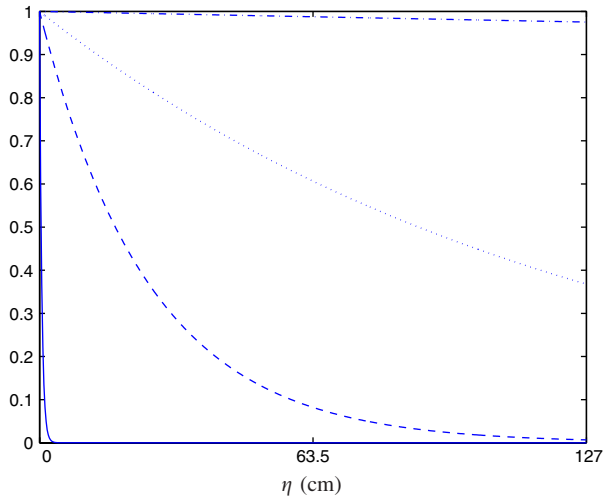

Fig. 7. Candidate spatial correlation models, $\phi(\eta;\theta_i) = \exp(-\theta_i|\eta|)$, for $\theta_1 = 5.0$ (solid), $\theta_2 = 0.1$ (dashed), $\theta_3 = 0.02$ (dotted), and $\theta_4 = 0.0005$ (dash-dot).

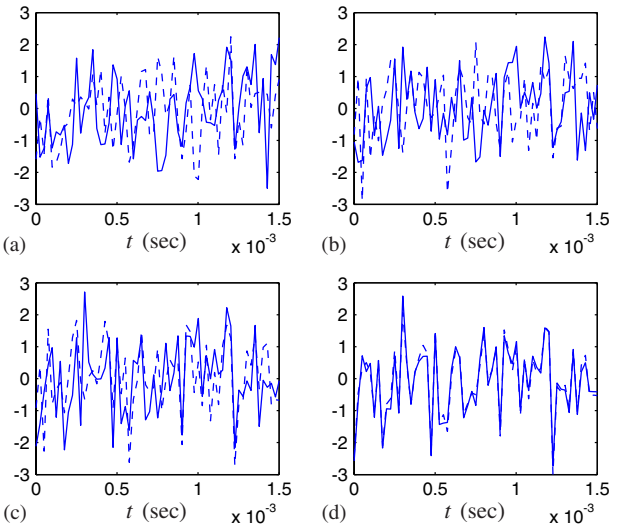

Fig. 8. One sample of Gaussian process, $G(x;t)$, at $x = 25.4\,\text{cm}$ (solid) and $x = 95.3\,\text{cm}$ (dashed) for: (a) $G|m_1$, (b) $G|m_2$, (c) $G|m_3$, and (d) $G|m_4$.

the latter being the attachment point for the oscillator. Note that as θ approaches zero, the samples of the processes $G(x_1;t)$ and $G(x_2;t)$, $x_1, x_2 \in [0, l]$, are nearly in phase.

4.2. Sensitivity of model output

One sample of the displacement response of the beam at the attachment point, $D(x = 95.25\,\text{cm};t)$, is shown in Fig. 9 for the case of $\bar{t} = 0.03$ and $\xi = 0.09\,\text{s}$. For calculations,

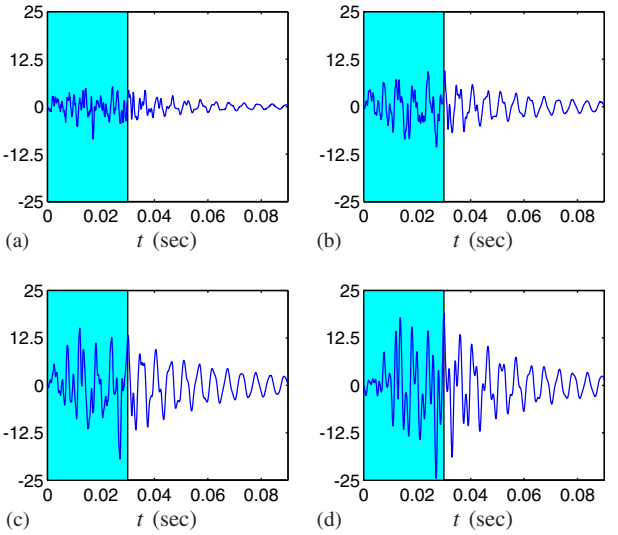

Fig. 9. One sample of beam response process in units of μm for: (a) $D|m_1$, (b) $D|m_2$, (c) $D|m_3$, and (d) $D|m_4$.

the input and response are discretized by a uniform time step of $1/2\bar{\omega} = 2.5 \times 10^{-5}$ s. The shaded area indicates the time interval when the load is applied, $t \in [0, \bar{t}]$; the unshaded area corresponds to free vibration, $t \in (\bar{t}, \xi]$. These plots show that the displacement response at the attachment point is very sensitive to the degree of spatial correlation on the input: as the spatial correlation increases (decreasing θ), the magnitude of the response increases.

Estimates of $(\max_x |D(x;t)|, \max_t |D(x;t)|)$, $x \in [0, l]$, $t \in [0, \xi]$, the joint distribution of the location and magnitude of the maximum displacement of the beam, are shown in Fig. 10 using results from 2000 Monte Carlo samples. For large θ (nearly uncorrelated in space), the range of observed values for $\max_x |D(x;t)|$ is large and they occur most frequently at the right end of the beam; the range of observed values for $\max_t |D(x;t)|$ is small in comparison. As θ decreases, the pattern is reversed. The range of observed values for $\max_x |D(x;t)|$ is small and they occur most frequently near the attachment point; the range of observed values for $\max_t |D(x;t)|$ is large in comparison. Similar patterns are observed for the acceleration response of the component, $\ddot{Y}(t)$. One sample of $\ddot{Y}(t)$ is shown in Fig. 11. As the degree of spatial correlation increases, so does the magnitude of the acceleration of the attached mass. Estimates of the variance of $\ddot{Y}(t)$ using results from 2000 Monte Carlo samples are shown in Fig. 12 for $t \in [0, \bar{t}]$.

Estimates of the distribution of $g(\ddot{Y})$ defined by Eq. (12), using results from 2000 Monte Carlo samples, are shown in Fig. 13. It is evident from the figure that assuming the input to be uncorrelated in space, which corresponds to the case where $\theta = 5.0$ (model m_1), is non-conservative, since the probability of exceeding a critical level of acceleration increases with decreasing θ.

For this 1-D model of the spacecraft, it has been demonstrated that predictions of beam displacement, $D(x;t)$, and acceleration of the mass, $\ddot{Y}(t)$, are sensitive to the degree of spatial correlation of the input, $Z(x;t)$. Specifically, as the degree of spatial correlation increases, the maximum in time of $D(x;t)$ and $\ddot{Y}(t)$ increase. In the general 3-D case, the input process $\mathbf{Z}(\mathbf{x};t)$

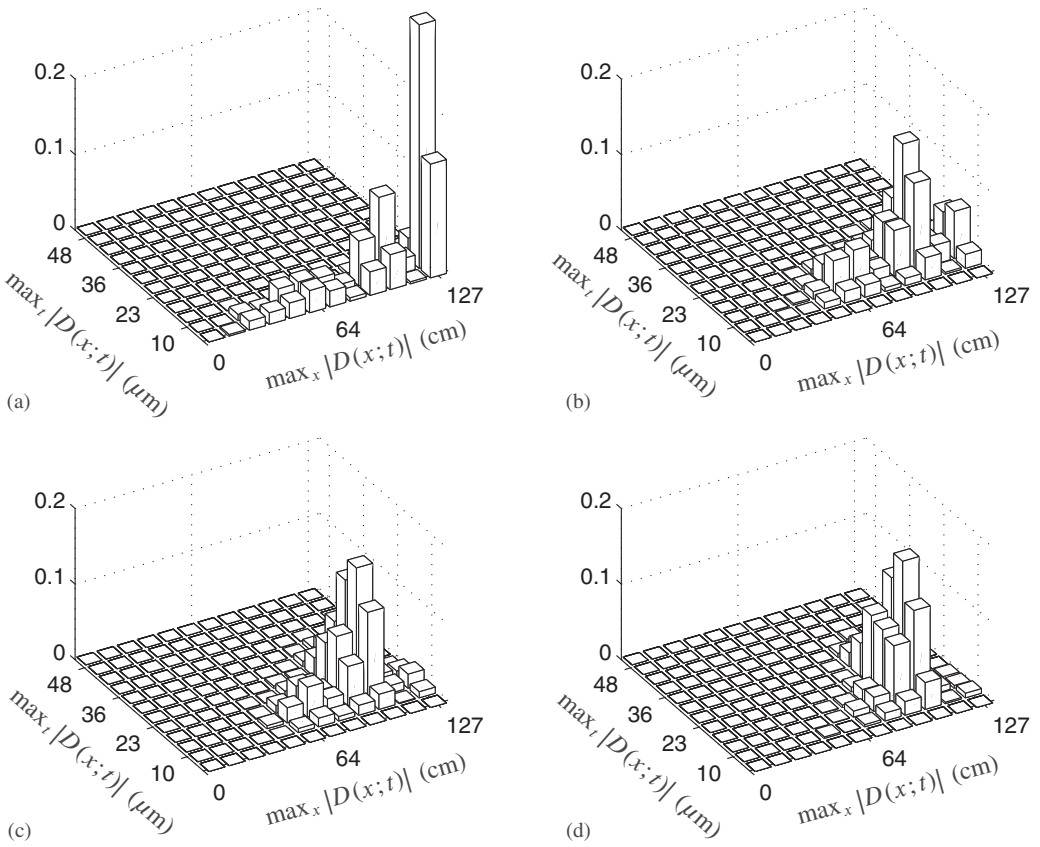

Fig. 10. Histogram of $(\max_x|D(x;t)|, \max_t|D(x;t)|)$ for: (a) $D|m_1$, (b) $D|m_2$, (c) $D|m_3$, and (d) $D|m_4$.

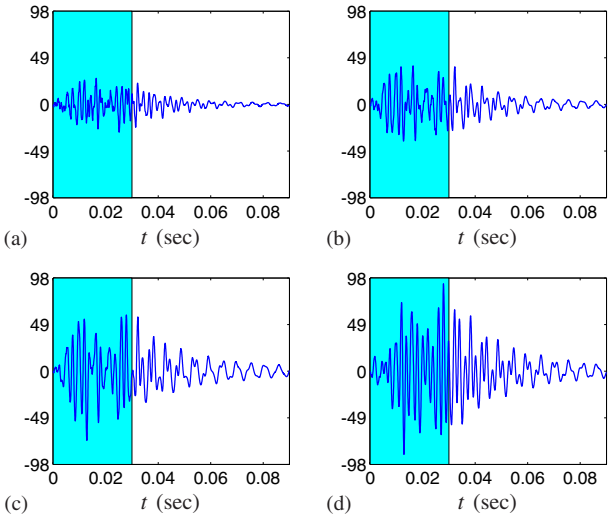

Fig. 11. One sample of component response in units of m/s^2 for: (a) $\ddot{Y}|m_1$, (b) $\ddot{Y}|m_2$, (c) $\ddot{Y}|m_3$, and (d) $\ddot{Y}|m_4$.

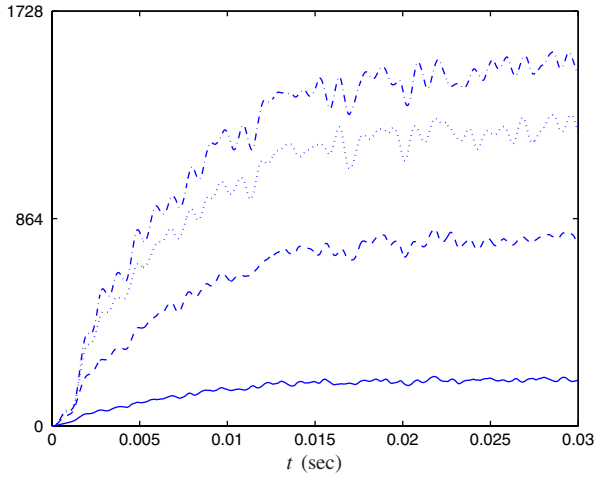

Fig. 12. Estimates of $\mathrm{Var}[\ddot{Y}(t)|m_1]$ (solid), $\mathrm{Var}[\ddot{Y}(t)|m_2]$ (dashed), $\mathrm{Var}[\ddot{Y}(t)|m_3]$ (dotted), and $\mathrm{Var}[\ddot{Y}(t)|m_4]$ (dash-dot), in units of $(\mathrm{m/s^2})^2$.

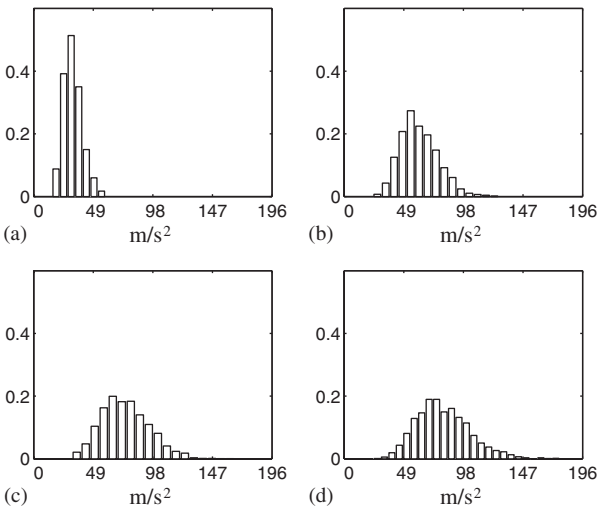

Fig. 13. Histograms of: (a) $g(\ddot{Y})|m_1$, (b) $g(\ddot{Y})|m_2$, (c) $g(\ddot{Y})|m_3$, and (d) $g(\ddot{Y})|m_4$.

exhibits spatial correlation in two directions (axial and hoop); the sensitivity of model output demonstrated will likely increase. It is therefore crucial to select optimal models for the spatial correlation of the input.

4.3. Optimal model

Here we select an optimal value for the spatial correlation parameter, θ. We begin with an analysis on the smaller class of candidate models, $\bar{\mathscr{M}}_1$ defined by Eq. (15), then use the results to approximate the optimal member from the larger, uncountable class, $\mathscr{M}_1$ defined by Eq. (14).

The objective is to assess the performance of the spacecraft in the re-entry environment via Eq. (13). Let

$$h_i(d) = P(g(\ddot{Y}) \leqslant d \mid m_i), \quad i = 1, 2, 3, 4, \tag{16}$$

denote the prediction of performance under model m_i, where d is the specified critical value for the acceleration of the mass, $\ddot{Y}$, and $g(\ddot{Y})$ is defined by Eq. (12). By Eq. (16), if $m_j \in \bar{\mathscr{M}}_1$ is true, the system performance is $h_j(d)$. In this case, we say that model m_i results in a conservative prediction of system performance if $h_i(d) \leqslant h_j(d)$. Likewise, m_i results in a non-conservative prediction of system performance if $h_i(d) > h_j(d)$. A conservative prediction is preferable to a non-conservative prediction.

Methods from decision theory [18] can be used to select the optimal model from $\bar{\mathscr{M}}_1$. These methods are used to quantify the consequences of choosing an inappropriate model for the input, Z, through the use of a utility function, U, where the objective is to select the model with the minimum expected utility [4,5]. Define

$$U(m_i, m_j) = \gamma(m_i) + \psi(m_i, m_j) \tag{17}$$

to be the utility of model m_i, when model m_j is true, where $\gamma(m_i) \geqslant 0$ denotes the cost of model m_i, and $\psi(m_i, m_j) \geqslant 0$ denotes the penalty associated with using model m_i, when model m_j is true. For example, we set $\gamma(m_i) > \gamma(m_k)$ if a prediction with model m_i requires additional resources, e.g., CPU time, than a prediction with model m_k, and $\psi(m_i, m_j) > \psi(m_k, m_j)$ if, assuming m_j is true, the consequences of a prediction with model m_k are preferable to the consequences of a prediction with model m_i.

The optimal model, $m^\star \in \bar{\mathscr{M}}_1$, is, such that

$$u(m^\star) \leqslant u(m_j), \quad j = 1, 2, 3, 4, \tag{18}$$

where

$$u(m_i) = E[U(m_i, \bar{\mathscr{M}}_1)] = \gamma(m_i) + \sum_{j=1}^{4} \psi(m_i, m_j) p_j, \tag{19}$$

is the expected utility of model m_i, and p_j denotes the probability that model m_j is true. For calculations, we consider the following penalty:

$$\psi(m_i, m_j) = \tilde{\psi}(h_i, h_j) = \begin{cases} \beta_1 [h_i(d) - h_j(d)]^2 & \text{if } h_i(d) \leqslant h_j(d), \\ \beta_2 [h_i(d) - h_j(d)]^2 & \text{if } h_i(d) > h_j(d), \end{cases} \tag{20}$$

where $\beta_2 > \beta_1 \geqslant 0$ are deterministic parameters. By Eq. (20), non-conservative predictions of system performance are heavily penalized; overly conservative predictions are also subject to penalty.

The expected utilities of the four models in $\bar{\mathscr{M}}_1$ are listed in Table 2 for three values of d; in each case, the optimal model, $m^\star$, is in bold. Parameters $\beta_1 = 1$ and $\beta_2 = 2$ were used for calculations. Each candidate model for Z is assumed equally likely and has no cost, i.e., $p_i = \frac{1}{4}$ and $\gamma(m_i) = 0$, $i = 1, 2, 3, 4$. For $d = 49\,\mathrm{m/s^2}$ (5 g) and $d = 98\,\mathrm{m/s^2}$ (10 g), models m_2 and m_3 are selected, corresponding to $\theta_2 = 0.1$ and $\theta_3 = 0.02$, respectively. Model m_1, corresponding to the case where the spatial correlation is nearly white noise, is never selected since the assumption that the input is

Table 2
Expected utilities of each $m_i \in \mathscr{M}_1'$

d (m/s^2)	Expected utilities			
	$u(m_1)$	$u(m_2)$	$u(m_3)$	$u(m_4)$
19.6	7.935×10^{-4}	$\mathbf{1.323 \times 10^{-4}}$	$\mathbf{1.323 \times 10^{-4}}$	$\mathbf{1.323 \times 10^{-4}}$
49	1.114	$\mathbf{1.670 \times 10^{-1}}$	2.057×10^{-1}	2.223×10^{-1}
98	3.203×10^{-2}	2.615×10^{-2}	$\mathbf{1.108 \times 10^{-2}}$	2.287×10^{-2}

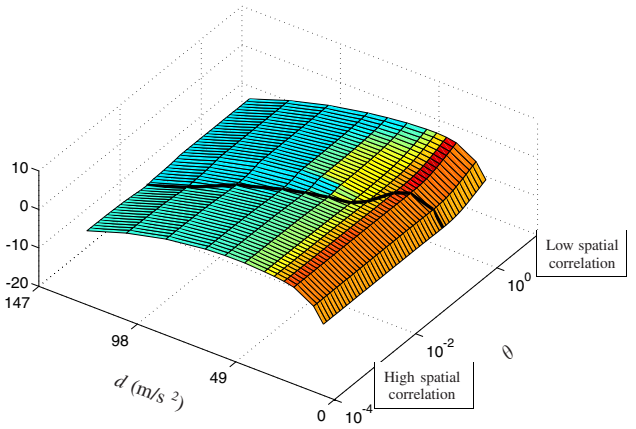

Fig. 14. Natural log of expected utilities, $\ln[u(\theta)]$, $\theta \in \mathscr{M}_1$.

uncorrelated in space leads to non-conservative predictions of system performance (see Fig. 13). For $d = 19.6\,\mathrm{m/s^2}$ (2 g), models m_2, m_3, and m_4 give identical estimates of the performance metric, so there is no preference of one model over another.

A surface defining the expected utility of each model can be defined over $1 \leqslant d \leqslant 14$ and $0.0005 \leqslant \theta \leqslant 5$, the latter being consistent with $\mathscr{M}_1$ defined by Eq. (14). This surface is shown in Fig. 14, where the natural logarithm of the expected utilities are plotted to emphasize the results. The minimum of the surface for each d gives an estimate of the optimal value for $\theta \in \mathscr{M}_1$. As d increases, the optimal model corresponds to an increasing degree of spatial correlation; the dependence on spatial correlation decreases with increasing d. The limiting cases of perfect and zero spatial correlation on the input are commonly used in practice; by Fig. 14, these assumptions are not optimal for any value for d.

4.4. Sensitivity of optimal model

We study the sensitivity of the optimal model to changes in the parameters of the penalty function, Eq. (20). To do so, define a normalized penalty function parameter $\bar{\beta} = \beta_2/\beta_1$. For $\bar{\beta} \gg 1$, non-conservative predictions of system performance are highly penalized with respect to

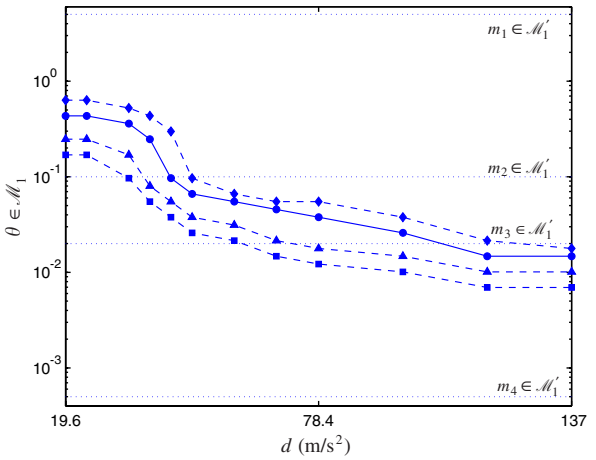

Fig. 15. Optimal $\theta \in \mathscr{M}_1$ versus d for $\bar{\beta} = 1.1$ (diamond), $\bar{\beta} = 2$ (circle), $\bar{\beta} = 5$ (triangle), and $\bar{\beta} = 10$ (square).

conservative predictions; as $\bar{\beta} \to 1$, the penalty for conservative and non-conservative models is identical.

The optimal models from $\mathscr{M}_1$ are plotted in Fig. 15 for various values for d. Four lines are plotted, which correspond to four different values for $\bar{\beta}$. The solid line ($\bar{\beta} = 2$) corresponds to the results of Section 4.3. The dotted lines correspond to the four models from $\bar{\mathscr{M}}_1$. In general, changing $\bar{\beta}$ shifts the curve up or down. As $\bar{\beta}$ increases, the penalty function defined by Eq. (20) becomes highly asymmetrical, and models with more spatial correlation (smaller θ) are favored. In all cases, the optimal spatial correlation parameter satisfies $0.005 \leqslant \theta \leqslant 0.5$, meaning that the limiting cases of perfect or zero spatial correlation are unfavorable, even for large changes in $\bar{\beta}$. Hence, precise values for β_1 and β_2 are not essential for a rational decision.

5. Model selection for marginal PDF of input

Recall Figs. 1 and 2, showing measured accelerations during the re-entry of the Space Shuttle Orbiter and wind-tunnel pressure measurements on an aircraft fuselage, respectively. In both plots, non-Gaussian behavior is clearly evident. In this section, we consider non-Gaussian models for the input, Z, i.e., Case #2; the decision-theoretic method for model selection is used to select the optimal member from a class of candidate models for Z.

We assume that: (1) the spatial correlation function of the input, ϕ, is perfectly known and equal to one, and (2) there is no feedback from the oscillator to the beam. Assumption (1) implies that Eq. (9) reduces to

$$Z(x;t) = \sigma_Z(x)Q(t), \quad t \in [0, \bar{t}], \tag{21}$$

where the dependence of Q on x is removed because it exhibits perfect spatial correlation. As a result, the second-moment properties of Z are now completely defined. All candidate models considered in this section are equivalent in the second-moment sense, but have different marginal

Table 3
Oscillator parameters

Parameter	Values	Units
b	31.75, 57.15, 95.25	cm
ω_c	2000, 2250, 5000	Hz

distributions. Because of assumption (2), the method for analysis is given by Eq. (8). This allows us to study the effects of the distribution of Z on $\ddot{Y}$ for various values of b, the location of the oscillator (see Fig. 5), and ω_c, the natural frequency of the oscillator.

Table 3 lists the values of the oscillator parameters used in the analyses that follow; the values for ω_c considered are consistent with observed resonant frequencies of, for example, small electronics packages, e.g., circuit boards. The damping ratio of the oscillator, $\zeta_c = 0.02$, as well as the parameters of the beam from Table 1, remain fixed. It can be shown that one of the resonant frequencies of the oscillator considered, $\omega_c = 2000\,\text{Hz}$, coincides with a resonant frequency of the beam (see Ref. [4, Section 5.3.3]).

5.1. Candidate models

Let

$$\mathscr{M}_2 = \{Z_i(x;t),\ i = 1,2,3,4\} = \{m_1, m_2, m_3, m_4\} \tag{22}$$

be the class of candidate models for the applied pressure field, where

$$Z_i(x;t) = \sigma_Z(x) Q_i(t), \tag{23}$$

Q_1 is a zero mean, unit variance, stationary Gaussian process with correlation function given by Eq. (10), Q_2 is a student-t translation process, and Q_3 and Q_4 are filtered Poisson processes. As previously stated, the processes Q_i, $i = 1,2,3,4$, are equal in the second-moment sense.

The translation process [19], Q_2, is given by

$$Q_2(t) = F^{-1} \circ \Phi[Q_1(t)], \tag{24}$$

where

$$F(z;r) = \frac{\Gamma(r+1/2)}{\sqrt{\pi r}\Gamma(r/2)} \int_{-\infty}^{\sqrt{r/(r-2)}z} \left[1 + \frac{t^2}{r}\right]^{-1/2(r+1)} \mathrm{d}t \tag{25}$$

is a student-t distribution with $(r-1)$ dof [20], Φ denotes the standard normal CDF, and $\Gamma(\cdot)$ denotes the Gamma function. A random variable with the distribution given by Eq. (25) has zero mean and unit variance; the process $Z_2(x;t) = \sigma_Z(x)Q_2(t)$ is therefore equivalent in the second-moment sense to $Z_1(x;t)$ for each r. $Z_2(x;t)$ can be assigned any coefficient of kurtosis greater than 3 without altering the second-moment properties via [21]

$$\mathrm{Kur}[Z_2] = \frac{3(r-2)}{r-4}, \quad r > 4. \tag{26}$$

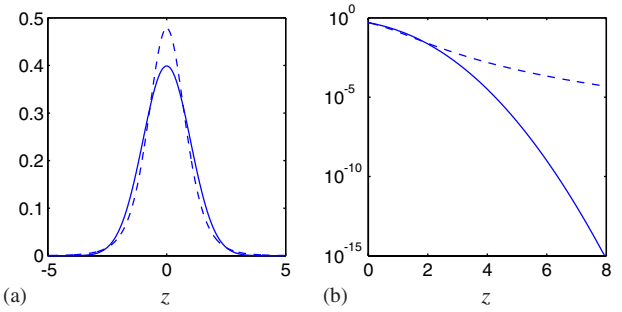

Fig. 16. The Gaussian (solid) and student-t distributions (dashed): (a) PDFs, and (b) tails.

The PDF of the student-t distribution with a coefficient of kurtosis of 7 ($r = \frac{11}{2}$), is plotted along with the Gaussian PDF in the left-hand side of Fig. 16. This distribution has heavier tails that of the Gaussian distribution, as illustrated further by the right-hand side of the figure; the Gaussian distribution has a coefficient of kurtosis of 3.

The third and fourth models considered are $Q_3(t) = V(t;\lambda_3)$ and $Q_4(t) = V(t;\lambda_4)$, where

$$V(t;\lambda) = \begin{cases} 0, & N(t) = 0, \\ \sum_{k=1}^{N(t;\lambda)} W_k f(t - T_k), & N(t) > 0, \end{cases} \tag{27}$$

is a type of filtered Poisson process [17, p. 78]. The process is characterized by pulses of deterministic shape and random magnitude, occurring at (random) Poisson times. $V(t)$ depends on $\{N(t;\lambda),\ t \geqslant 0\}$, a homogeneous Poisson counting process of intensity $\lambda > 0$, independent identically distributed (i.i.d.) random variables $\{W_k,\ k \geqslant 1\}$, with mean zero and variance σ^2, the random times, $\{T_k,\ k \geqslant 1\}$, at which the Poisson events occur, and the deterministic shape function, $f(t)$, $t \geqslant 0$. The process $N(t)$ has the property that $E[N(t)] = \lambda t$ so that $\lambda = E[N(t)]/t$ represents the average number of pulses per unit time [22]. With proper choice of $f(t)$, σ^2, and λ, models $Z_3(x;t)$ and $Z_4(x;t)$ are equivalent to $Z_1(x;t)$ and $Z_2(x;t)$ in the second-moment sense (see Ref. [17, Section 3.3]). For small λ, the pulses have large magnitudes and occur infrequently. As λ increases, the pulses occur more frequently, but with smaller magnitude; as $\lambda \to \infty$, the marginal distribution of $V(t)$ becomes Gaussian [17].

One sample of the Gaussian process, $Q_1(t) = G(t)$, the translation process, $Q_2(t) = F^{-1} \circ \Phi[G(t)]$, and the two filtered Poisson processes, $Q_3(t) = V(t;\lambda_3)$ and $Q_4(t) = V(t;\lambda_4)$ with $\lambda_3 = 10,000$ and $\lambda_4 = 100,000$, respectively, are plotted in Fig. 17. Samples from the four models look quite different, but each is consistent with all available information, i.e., they each have the specified second-moment properties. Estimates of the marginal PDFs of Q_3 and Q_4 using 500 samples are shown in Fig. 18. Also shown is the marginal PDF of Q_1.

5.2. Sensitivity of model output

One sample of the acceleration of the mass, $\ddot{Y}(t)$, is shown in Fig. 19; the four plots correspond to the four models of the applied pressure field for the case of $b = 31.75$ cm (12.5 in) and

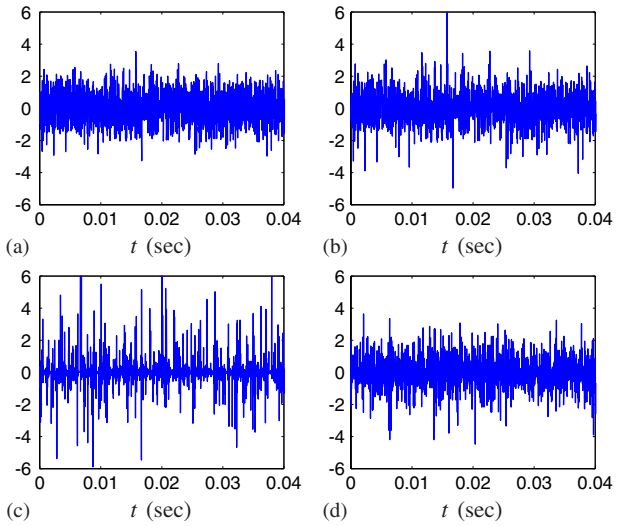

Fig. 17. One sample of: (a) $Q_1(t)$, (b) $Q_2(t)$, (c) $Q_3(t)$, and (d) $Q_4(t)$.

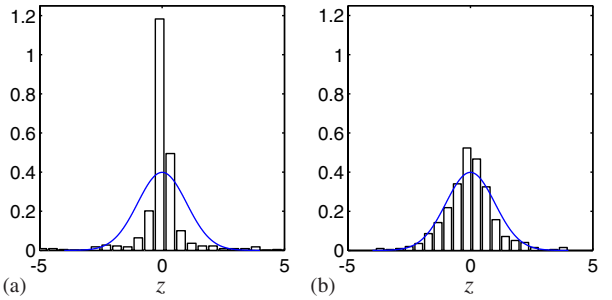

Fig. 18. Marginal PDFs of filtered Poisson (bar) and Gaussian process (solid line) for: (a) $\lambda_3 = 10,000$ and (b) $\lambda_4 = 100,000$.

$\omega_c = 5000\,\text{Hz}$. The shaded area indicates the time interval when the load is applied, $t \in [0, \bar{t} = 0.05\,\text{s}]$; the unshaded area corresponds to free vibration, $t \in [\bar{t}, \xi]$. $\ddot{Y}$ is the output from a linear filter. Because of this, and the fact that all inputs considered are equivalent in the second-moment sense, the outputs will have identical second-moment properties [17].

As previously discussed, the probability laws for $m_i \in \mathscr{M}_2$ are different; the resulting probability laws for $\ddot{Y}(t)$, and hence the performance metric defined by Eq. (13) will therefore also differ. To illustrate, we define

$$h_i(\hat{\sigma}d) = P(g(\ddot{Y}) \leqslant \hat{\sigma}d \,|\, m_i), \quad i = 1, 2, 3, 4. \tag{28}$$

The quantity $\hat{\sigma}$ is the estimated steady-state standard deviation of $\ddot{Y}(t)$ and is used to normalize the tail estimates; $g(\ddot{Y})$ is defined by Eq. (12). We note that it is possible to calculate the true value for the standard deviation of $\ddot{Y}(t)$ from the covariance equation, but the large dimension of Eq. (8a) proved prohibitive. Estimates of Eq. (28) are illustrated by Fig. 20 for two cases:

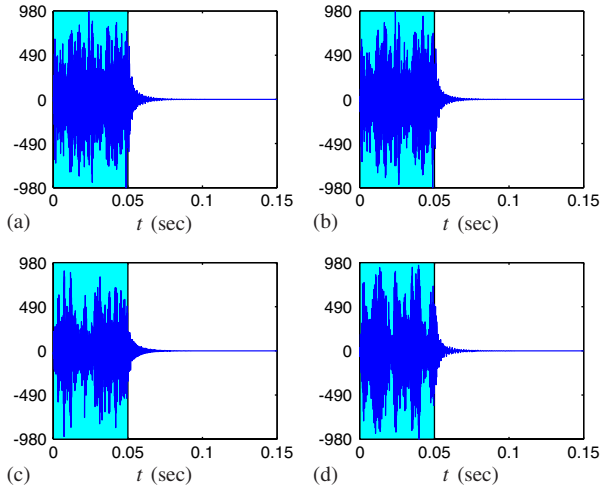

Fig. 19. One sample of component response in units of m/s^2 for: (a) $\ddot{Y}|m_1$, (b) $\ddot{Y}|m_2$, (c) $\ddot{Y}|m_3$, and (d) $\ddot{Y}|m_4$.

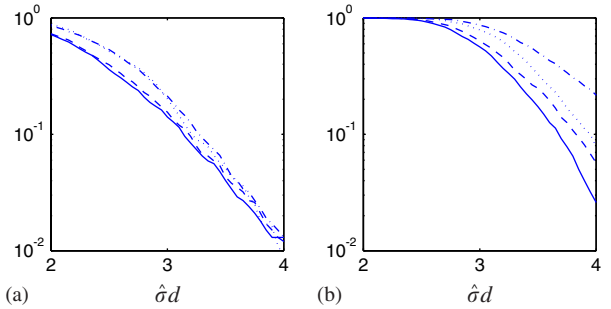

Fig. 20. Estimates of $1 - h_i(\hat{\sigma}d)$ for $i = 1$ (solid), $i = 2$ (dashed), $i = 3$ (dash-dot), and $i = 4$ (dotted). Two cases are considered: (a) $b = 95.25\,\text{cm}$, $\omega_c = 2000\,\text{Hz}$, and (b) $b = 31.75$ cm, $\omega_c = 5000\,\text{Hz}$.

(1) $b = 95.25\,\text{cm}$ (37.5 in), $\omega_c = 2000\,\text{Hz}$ (left), and (2) $b = 31.75\,\text{cm}$ (12.5 in), $\omega_c = 5000\,\text{Hz}$ (right). As shown by the plot on the right, models m_2, m_3, and m_4, in general, provide conservative estimates of Eq. (28) with respect to the Gaussian model, m_1. Model m_3 is the most conservative, due to the fact that Z_3 exhibits the heaviest tail. For $\omega_c = 2000\,\text{Hz}$, a resonant frequency of the beam, the tail estimates are nearly identical, as shown in the left-hand side of Fig. 20. The response of the oscillator is insensitive to the tails of $Z(x;t)$ when ω_c coincides with a resonant frequency of the beam.

The magnitude of the difference between the tails of the distributions shown in Fig. 20 is sensitive to changes in parameters b and ω_c. To illustrate, we define

$$\rho(\hat{\sigma}d) = \max_i |h_1(\hat{\sigma}d) - h_i(\hat{\sigma}d)|, \quad i = 2, 3, 4. \tag{29}$$

Eq. (29) is plotted on the left-hand side of Fig. 21 for the case of $\hat{\sigma}d = 4$ and different values for b and ω_c. The shading of the bars denotes which model maximizes ρ; in seven of the nine cases

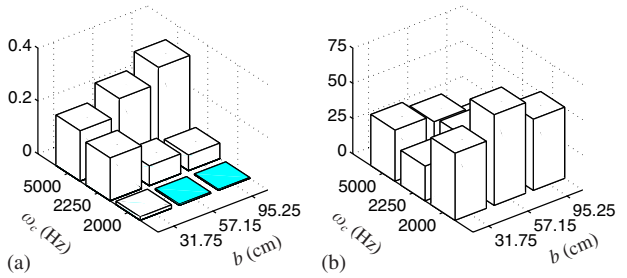

Fig. 21. Estimates of: (a) $\rho(\hat{\sigma}d = 4)$ and (b) $\hat{\sigma}$; $\hat{\sigma}$ is in units of g.

considered, it is m_3 (unshaded), while it is m_2 in the remaining two cases (shaded). In general, for increasing b, ρ may increase or decrease. As the frequency of the oscillator is increased, ρ increases; for $\omega_c = 2000\,\text{Hz}$, a resonant frequency of the beam, ρ is near zero for all values for b considered. Hence, the sensitivity to the tails of Z can be minimized by placing ω_c near a resonant frequency of the beam. Of course, this has the undesirable effect of increasing the variance of the response, as depicted by the right-hand side of Fig. 21.

It has been demonstrated that predictions of component acceleration, $\ddot{Y}$, are sensitive to the tails of the marginal distribution of the input, Z, when the oscillator natural frequency, ω_c, does not coincide with a resonant frequency of the beam. As the tail of the marginal PDF of the input model becomes heavier, the maximum in time of $\ddot{Y}(t)$ increases. A Gaussian model for Z can therefore give non-conservative predictions of system performance.

5.3. Optimal model

In this section, we use the decision-theoretic method for model selection to select the optimal marginal distribution of the input pressure field from the class of candidate models defined by Eq. (22).

The penalty function used in the analysis is unchanged from the previous section, i.e., Eq. (20). However, the computational effort associated with each model in $\mathscr{M}_2$ is no longer identical; the costs, $\gamma(m_i)$, $i = 1, 2, 3, 4$, defined by Eq. (17) must reflect this. Table 4 lists the average CPU times required to calculate one sample of each of the four candidate models in $\mathscr{M}_2$. Samples of the Gaussian process, m_1, can be calculated with the least effort; the filtered Poisson process with $\lambda_3 = 10,000$, m_3, requires slightly more. Samples of the filtered Poisson process with $\lambda_4 = 100,000$, m_4, take approximately 10 times longer to generate than either m_1 or m_3. The corresponding costs, scaled by deterministic parameter $\gamma_0 > 0$, are listed in Table 4. In each case, $\gamma(m_i)/\gamma_0$ is the average CPU time of m_i, normalized by the CPU time of m_1 (the fastest).

Table 5 lists the expected utilities of each $m_i \in \mathscr{M}_2$ using Eq. (19). Results for the different values of b, the location of the oscillator, and ω_c, the resonant frequency of the oscillator, are shown for $\hat{\sigma}d = 4$. Parameters $\beta_1 = 1$, $\beta_2 = 2$, and $\gamma_0 = 0.05$ were used for calculations. The translation process, m_2, is selected most often; the cost of m_2 is not significantly greater than that of m_1, and it, in general, provides slightly conservative estimates of $P(g(\ddot{Y}) \leqslant d)$. The filtered Poisson process with $\lambda = 10,000$, m_3, is selected only twice; it provides overly conservative estimates of system performance in many cases. The Gaussian model, m_1, is selected only for the

Table 4
Average CPU times and costs

Model	CPU time (s)	Cost, $\gamma(m_i)$
m_1	0.6558	γ_0
m_2	1.025	$1.563\gamma_0$
m_3	0.6886	$1.050\gamma_0$
m_4	6.114	$9.323\gamma_0$

Table 5
Expected utilities of each $m_i \in \mathscr{M}_2$

b (cm)	ω_c (Hz)	$u(m_1)$	$u(m_2)$	$u(m_3)$	$u(m_4)$
31.75	2000	$\mathbf{5.109 \times 10^{-3}}$	7.924×10^{-3}	5.344×10^{-3}	4.666×10^{-2}
31.75	2250	1.854×10^{-2}	$\mathbf{1.800 \times 10^{-2}}$	2.182×10^{-2}	5.667×10^{-2}
31.75	5000	2.507×10^{-2}	$\mathbf{2.108 \times 10^{-2}}$	2.560×10^{-2}	5.706×10^{-2}
57.15	2000	$\mathbf{5.013 \times 10^{-3}}$	7.830×10^{-3}	5.265×10^{-3}	4.667×10^{-2}
57.15	2250	8.294×10^{-3}	1.006×10^{-2}	$\mathbf{8.209 \times 10^{-3}}$	4.796×10^{-2}
57.15	5000	4.013×10^{-2}	$\mathbf{3.061 \times 10^{-2}}$	4.317×10^{-2}	6.811×10^{-2}
95.25	2000	$\mathbf{5.003 \times 10^{-3}}$	7.819×10^{-3}	5.254×10^{-3}	4.664×10^{-2}
95.25	2250	7.085×10^{-3}	9.276×10^{-3}	$\mathbf{7.060 \times 10^{-3}}$	4.742×10^{-2}
95.25	5000	5.810×10^{-2}	$\mathbf{3.972 \times 10^{-2}}$	6.699×10^{-2}	9.117×10^{-2}

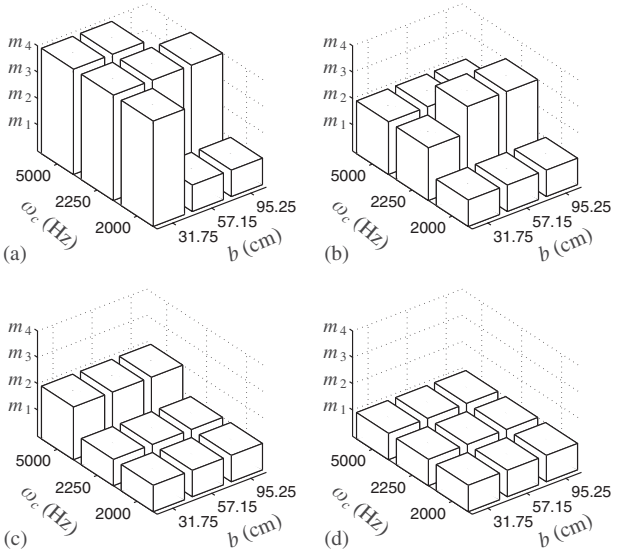

Fig. 22. Sensitivity of $m^\star$ to changes in cost parameter: (a) $m^\star|\gamma_0 = 0$, (b) $m^\star|\gamma_0 = 0.005$, (c) $m^\star|\gamma_0 = 0.01$, and (d) $m^\star|\gamma_0 \to \infty$.

case when $\omega_c = 2000$ Hz, i.e., when the oscillator frequency coincides with a resonant frequency of the beam. This is because the tail estimates nearly coincide here (see Fig. 20), and the cost term dominates the utility. Model m_4 provides slightly conservative estimates of system performance, but is never selected due to its large computational cost (see Table 4).

5.4. Sensitivity of optimal model

We consider the sensitivity of the optimal model to changes in parameter γ_0, the weight on the cost. For $\gamma_0 = 0$, the computational costs of the models are ignored in the model selection process; as $\gamma_0 \to \infty$, the cost dominates the model selection process. Fig. 22 shows the optimal model, denoted by $m^\star$, for each value of b and ω_c considered, for four values of γ_0. The case where $\gamma_0 = 0.005$ corresponds to the results of Table 5. For $\gamma_0 = 0$, computational cost is ignored, and model m_4 is selected most often. As γ_0 increases, the Gaussian model, m_1, is optimal for any b and ω_c.

6. Conclusions

A method for selecting optimal models for the environment during atmospheric re-entry of a spacecraft was developed. The method was based on a decision-theoretic approach for selecting the optimal member from a collection of candidate models for the environment under limited information. Two cases were considered. First, the environment was assumed Gaussian with partially defined second-moment properties. Second, the environment was assumed to be completely defined in the second-moment sense, but with an unknown marginal distribution function. For each case, a collection of candidate models was considered, where each model in the collection was consistent with the available information. The optimal model in the collection minimized a postulated utility function. It was found that: (1) the often-used assumptions of perfect or zero spatial correlation on the input process were unfavorable, (2) non-Gaussian models for the input were sometimes optimal, and (3) results can be sensitive to the utility function.

Acknowledgements

This work was supported by Sandia National Laboratories. Sandia is a multiprogram laboratory operated by Sandia Corporation, a Lockheed Martin Company, for the United States Department of Energy's National Nuclear Security Administration under Contract DE-AC04-94AL85000.

References

[1] J. Martin, *Atmospheric Reentry: An Introduction to its Science and Engineering*, Prentice-Hall, Englewood Cliffs, NJ, 1966.

[2] L. Ely, *Return from Space: An Explanation of Re-entry Problems and Factors of Re-entry Vehicle Design and Performance*, Charles C. Thomas Publisher, Springfield, IL, 1966.

[3] J. Cockburn, J. Robertson, Vibration response of spacecraft shrouds to in-flight fluctuating pressures, *Journal of Sound and Vibration* 33 (4) (1974) 399–425.
[4] R. Field Jr., Methods for Model Selection in Applied Science and Engineering, PhD Thesis, Cornell University, 2004.
[5] M. Grigoriu, D. Veneziano, C. Cornell, Probabilistic modeling as decision making, *Journal of Engineering Mechanics* 105 (4) (1979) 585–596.
[6] M. Bull, Wall-pressure fluctuations beneath turbulent boundary layers: some reflections on forty years of research, *Journal of Sound and Vibration* 190 (3) (1996) 299–315.
[7] I. Elishakoff, A.T. van Zanten, S.H. Crandall, Wide-band random axisymmetric vibration of cylindrical shells, *Journal of Applied Mechanics* 46 (1979) 417–422.
[8] I. Elishakoff, *Probabilistic Theory of Structures*, Dover, New York, 1999.
[9] R. Blanchard, J. Nicholson, Orbiter rarefied-flow reentry measurements from the OARE on STS-62, Technical Report TM-110182, NASA, 1995.
[10] M. Hetényi, *Beams on Elastic Foundation*, The University of Michigan Press, 1983.
[11] L. Bergman, J. Nicholson, Stationary response of combined linear dynamic systems to stationary excitation, *Journal of Sound and Vibration* 103 (2) (1985) 225–236.
[12] R. Craig Jr., *Structural Dynamics*, Wiley, New York, NY, 1981.
[13] M. Greenberg, *Advanced Engineering Mathematics*, vol. 2, Prentice-Hall, Upper Saddle River, NJ, 1998.
[14] T. Soong, M. Grigoriu, *Random Vibration of Mechanical and Structural Systems*, PTR Prentice-Hall, Englewood Cliffs, NJ, 1993.
[15] A. Laganelli, A. Martellucci, L. Shaw, Wall pressure fluctuations in attached boundary-layer flow, *AIAA Journal* 21 (4) (1983) 495–502.
[16] B. Hassan, Estimation of fluctuation pressures on a sphere-cone geometry at hypersonic speeds, Technical Report, Sandia National Laboratories, September 2001.
[17] M. Grigoriu, *Applied Non-Gaussian Processes*, PTR Prentice-Hall, Englewood Cliffs, NJ, 1995.
[18] H. Chernoff, L. Moses, *Elementary Decision Theory*, Dover Publications, New York, NY, 1959.
[19] M. Grigoriu, Crossings of non-Gaussian translation processes, *Journal of Engineering Mechanics* 110 (1984) 610–620.
[20] A. Ang, W. Tang, *Probability Concepts in Engineering Planning and Design*: *Basic Principles*, vol. 1, Wiley, New York, NY, 1975.
[21] C. Kafali, M. Grigoriu, Non-Gaussian model for spatially coherent seismic ground motions, in: A.D. Kiureghian, S. Madanat, J. Pestana (Eds.), *Applications of Statistics and Probability in Civil Engineering*, Millpress, San Francisco, CA, 2003, pp. 321–327.
[22] S. Resnick, *Adventures in Stochastic Processes*, Birkhäuser, Boston, 1992.